University of Mississippi

eGrove

Faculty and Student Publications

Engineering, School of

11-1-2020

Wetting-driven formation of present-day loess structure

Yanrong Li
Taiyuan University of Technology

Weiwei Zhang
Taiyuan University of Technology

Shengdi He
Taiyuan University of Technology

Adnan Aydin
University of Mississippi

Follow this and additional works at: https://egrove.olemiss.edu/engineering_facpubs

 Part of the Biomedical Engineering and Bioengineering Commons, Chemical Engineering Commons, Civil and Environmental Engineering Commons, Computer Engineering Commons, Electrical and Computer Engineering Commons, Geological Engineering Commons, and the Mechanical Engineering Commons

Recommended Citation

Li, Y., Zhang, W., He, S., & Aydin, A. (2020). Wetting-driven formation of present-day loess structure. Geoderma, 377, 114564. https://doi.org/10.1016/j.geoderma.2020.114564

This Article is brought to you for free and open access by the Engineering, School of at eGrove. It has been accepted for inclusion in Faculty and Student Publications by an authorized administrator of eGrove. For more information, please contact egrove@olemiss.edu.

Geoderma 377 (2020) 114564

Contents lists available at ScienceDirect

Geoderma

journal homepage: www.elsevier.com/locate/geoderma

Wetting-driven formation of present-day loess structure

Yanrong Li[a,*], Weiwei Zhang[a], Shengdi He[a], Adnan Aydin[b]

[a] Department of Earth Sciences and Engineering, Taiyuan University of Technology, Taiyuan 030024, China
[b] Department of Geology and Geological Engineering, University of Mississippi, University MS 38677, USA

ARTICLE INFO

Handling editor name Yvan Capowiez

Keywords:
Initial loess
Present-day loess
Loess structural evolution
Wetting-driven cracking

ABSTRACT

Present-day loess, especially Malan loess formed in Later Quaternary, has a characteristic structure composed of vertically aligned strong units and weak segments. Hypotheses describing how this structure forms inside original loess deposits commonly relate it to wetting-drying process. We tested this causal relationship by conducting unique experiments on synthetic samples of initial loess deposits fabricated by free-fall of loess particles. These samples were subjected to a wetting-drying cycle, and their structural evolutions were documented by close-up photography and CT scanning. Analysis of these records revealed three key stages of structural evolution: initiation (evenly distributed cracks appear due to wetting); inhomogeneitization (some cracks grow, forming large polygons); and development (polygon-forming cracks grow further - cracks within polygons narrow down or heal up). These experiments successfully reproduced the characteristic structure of present-day loess, and led to a discovery that it is the wetting of initial loess that initiates and drives the structural evolution, while drying preserves and expands resulting features.

1. Introduction

Steep walls, columns, vertical joints, and cracks (Fig. 1a) are well developed in natural loess, especially Malan (Q_3) loess (Li et al., 2018b; Liu, 1985; Richthofen, 1882). Based on these observations, Li et al. (2018c) studied the geometrical and spatial characteristics of structural blocks in present-day loess and proposed the term “vertiloess” to refer to the characteristic structure in which vertically aligned strong units are coupled with weak segments (Fig. 1b). The strong units are composed of loess aggregates, fragments, and lumps that are held together by force chains (Fig. 1c), while the weak segments consist of pipes and cracks (Fig. 1d). The vertiloess, which imparts anisotropy to loess, well embodies the overall structural characteristics of present-day loess.

The vertiloess structure is a product of both syndepositional and postdepositional processes (Berg, 1916; Pécsi, 1990; Sprafke and Obreht, 2016). Under aeolian environment, dust particles deposited freely under gravity (Assallay et al., 1997; Ding et al., 2001), forming the initial loess deposit (ILD) (Pye, 1995; Smalley et al., 2016). The ILD possesses a metastable packing structure characterized by high void ratio and isotropic properties (Smalley et al., 2016). However, how this structure evolved into the present vertiloess structure is poorly understood.

Various factors have been considered as promoting the said structural evolution, including biological processes, overlying loads, freezing-thawing (FT) cycles, and wetting-drying (WD) cycles (Keith and Peter, 1982; Xu et al., 2017). Biological processes, such as root intrusion due to plant growth and post-death root decomposition, lead to tubular macropore formation (Richthofen, 1882). However, vegetation was scarce in most areas receiving loess materials during the accumulation periods (Liu, 1985) and there were no root traces in most pores of present-day loess (Pan, 1958). The overlying loads due to later deposition cause deformation and failure of macropores, which eventually result in smaller pore size (Li and Li, 2017). FT cycles likely lead to fragmentation of soil skeleton and homogenization of particle size and structure (Li et al., 2018a). Therefore, these processes may have only limited contribution to the formation of vertiloess structure, if any. On the other hand, WD cycles can lead to expansion or contraction of some clay minerals in soil (Pires et al., 2008), dissolution and precipitation of soluble salts (Zhang et al., 2013, 2014; Gao, 1988; Li et al., 2018d), relocation of particles (Lu et al., 2015), modification of interparticle forces (Li et al., 2014; Pires et al., 2008; Smalley et al., 2016) and improvement of pore connectivity (Pires et al., 2020). As such, the formation of vertiloess structure is most likely related to WD processes (e.g., downward infiltration and upward evaporation). This is consistent with observations that large structural blocks in present-day loess are elongated and vertically or sub-vertically aligned (Li et al., 2018c), and that macroscopic pores and pipes are mostly developed in the leaching zone at the upper part of loess profile (Pan, 1958).

* Corresponding author.
E-mail address: li.dennis@hotmail.com (Y. Li).

https://doi.org/10.1016/j.geoderma.2020.114564
Received 15 January 2020; Received in revised form 25 June 2020; Accepted 28 June 2020
Available online 17 July 2020
0016-7061/ © 2020 The Authors. Published by Elsevier B.V. This is an open access article under the CC BY-NC-ND license (http://creativecommons.org/licenses/BY-NC-ND/4.0/).

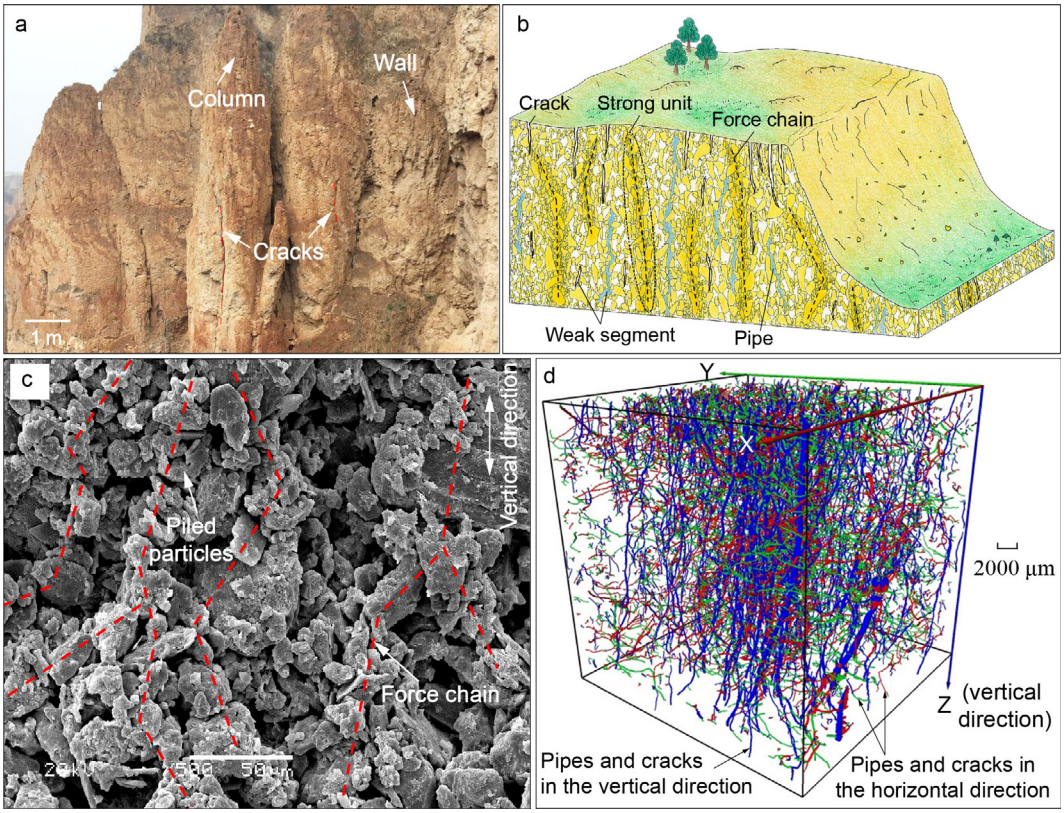

Fig. 1. Structural characteristics of present-day loess. a, Walls, columns, and cracks in a typical loess profile. b, A schematic diagram of the vertiloess structure, a combination of vertically aligned strong units and weak segments (Li et al., 2018c). c, A vertical cross-sectional SEM image of loess with an example of a force chain (Li et al., 2018c). d, Preferential vertical orientations (blue) of pipes and cracks visualized by CT images with a resolution of 59 μm (Li et al., 2018b). (For interpretation of the references to color in this figure legend, the reader is referred to the web version of this article.)

Several experiments on undisturbed loess or compacted loess soil have been conducted in recent years to investigate the modification of present-day loess structure by WD cycles. Results showed that WD cycles promoted volume expansion, increase of macropore number, propagation of original cracks (Peth et al., 2010), and development of new cracks (Li et al., 2014; Peth et al., 2010). However, the formation of present-day loess structure is hardly deciphered because of limitations in the tested samples. For this reason, we conducted WD experiments on reconstructed ILD in order to shed better light on the syndepositional-to-postdepositional structural development of loess.

2. Materials and methods

2.1. Fabrication of analog initial loess deposit (ILD)

The loess materials used for the fabrication of the ILD analogs were collected in Yuci City (37° 43′ 27″ N, 112° 47′ 38″ E), Shanxi Province at eastern Loess Plateau of China. This region has a typical temperate continental arid climate with an annual mean temperature of 8.7 °C and an annual mean rainfall of 396 mm. The field samples were taken at 3 m depth of a loess profile to avoid the plant roots. The content of organic matter (OC) in the sample was tested according to Chinese test method (GB/T 50123-2019) and found it was less than 0.01%. Considering the low OC content and the daily humid variation of the air, the field samples were oven dried at 50 °C for 24 h, and gently pulverized with a soft rubber mallet, avoiding excessive particle breakage (BS 1377-1:2016).

Chinese standard (GB/T 50123-2019) divides clay, silt and sand fractions with particle sizes of 0.005 mm, 0.075 mm and 2 mm, respectively. Based on the particle size distribution analysis, it was found that the above three fractions account for 17.73%, 78.48%, and 3.79%, respectively, in the field samples. This indicates that particles smaller than 0.075 mm account for the majority (96.21%). In order to achieve a relatively uniform ILD analogs without disturbance of large particles, the soil samples were passed through a 0.075 mm sieve.

Inspired by the airfall method of Assallay et al. (1997), we developed an ILD fabrication setup composed of a plexiglass sample cylinder and a sieve with aperture of 0.075 mm (Fig. 2a). Three sample cylinders were prepared: No. 1 cylinder (inner diameter Φ = 23 cm, height H = 24 cm) was used to prepare samples for the WD experiments. Nos. 2 and 3 (Φ = 5 cm, H = 5 cm and Φ = 2 cm, H = 2 cm) were used in the sample preparation for CT scanning. The sieve was placed 75 cm above these cylinders (Assallay et al., 1997), then the loess materials were sprayed onto this sieve, allowing free-fall of particles into the cylinders via mechanically shaking the sieve. Three sets of replicate samples were prepared and tested. The dry density of the analog ILD samples (Fig. 2a) was 0.88 g/cm^3 and the void ratio was 2.07. The particle density was 2.70 g/cm^3, which was obtained via the pycnometer method (GB/T 50123-2019).

Samples prepared in No. 2 (named ILD-5, 5 cm in diameter and 5 cm in height) and No. 3 (ILD-2, 2 cm in both diameter and height) cylinders were subjected to CT scanning for examination of the original structure of ILD.

2.2. Wetting-drying experiments

The analog ILD (No. 1 cylinder) was subjected to a WD cycle. Wetting and drying were realized by a spray nozzle simulating rainfall and a heating plate simulating evaporation, respectively (Fig. 2b). Deionized water was used for the experiment. The rainfall area of the nozzle was larger than the top surface of the ILD sample in order to maximize the homogeneous distribution of rainwater on the ILD

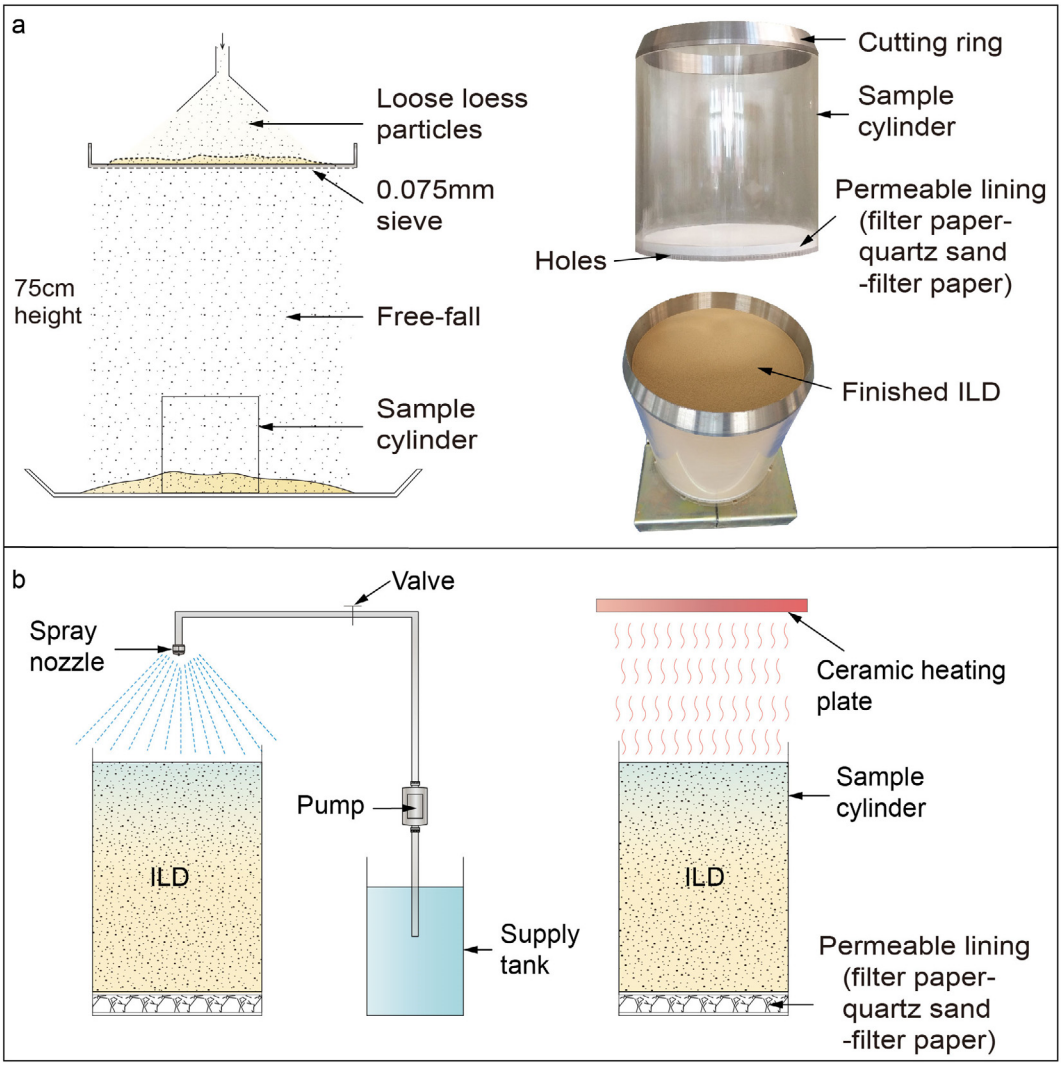

Fig. 2. Sample fabrication and experimental setups. a, The setup used in fabrication of ILD samples (modified from Assallay et al. (1997)). The bottom of the sample cylinder has 1 mm diameter holes, spaced 5 mm apart. A permeable lining layer (filter paper-quartz sand-filter paper) is laid over the holes. A cutting ring mounted on top of the cylinder prevents accumulation along the edge. b, Rainfall (left) and evaporation (right) setups simulate wetting and drying processes.

surface. Rainfall intensity and evaporation temperature were set at 10 mm/h and 30 °C, respectively, simulating the typical late Pleistocene climate of the Chinese Loess Plateau (Balsam et al., 2004; Liu, 1985; Liu et al., 2016; Meng et al., 2015). The rainfall process was continued until the wetting front reached the bottom of the sample cylinder and water started flowing out. Likewise, the evaporation process was continued until the sample was dried to a constant mass. To record the structural evolution, photos of the top and sides of the sample were taken at regular intervals. After the WD process, two cylindrical specimens (WD-5 and WD-2; numbers refer to the diameter and height in cm of the specimens) were taken from the center of the sample for subsequent structure examination.

2.3. CT scanning

The CT scanning was made by a nanoVoxel-4000 CT scanner produced by Sanying Precision Instruments Co., Ltd. A pre-filter was used to filter out low-energy rays in order to minimize beam hardening during the scanning procedure. After scanning, the program Voxelscan was used to reconstruct the complete 3D model of the sample. This program was developed by the scanner producer based on FDK analytical reconstruction algorithm. The reached voxel resolution is 35.7 μm × 35.7 μm × 35.7 μm for Samples ILD-5 and WD-5, and 18.56 μm × 18.56 μm × 18.56 μm for Samples ILD-2 and WD-2. The numbers of image slices were 1,400 and 1,077 for ILD-5/WD-5 and ILD-2/WD-2, respectively.

The structural parameters of pores and cracks were derived from these CT images. The parameters used for pores included diameter, circularity, convexity, aspect ratio, and pore volume, while crack parameters included length, width and tortuosity (Kapur et al., 1985; Li et al., 2018b; Malvern Instruments Ltd, 2013). The definitions and methods of quantification of these parameters are provided in the Supplementary Note.

3. Results

Three replicate samples have been tested via WD process. All three tests discovered the same pattern of structure evolution due to WD process. One of them was taken as representative and presented below.

3.1. Structural evolution driven by wetting

The structural evolution of ILD during WD cycle is shown in Figs. 3 and 4. Before WD, the ILD was loose and homogeneous (Fig. 3a). The size of pores was uniform (Fig. 4a–d). These pores were mostly sub-rounded with smooth edges, circularity greater than 0.8 and convexity

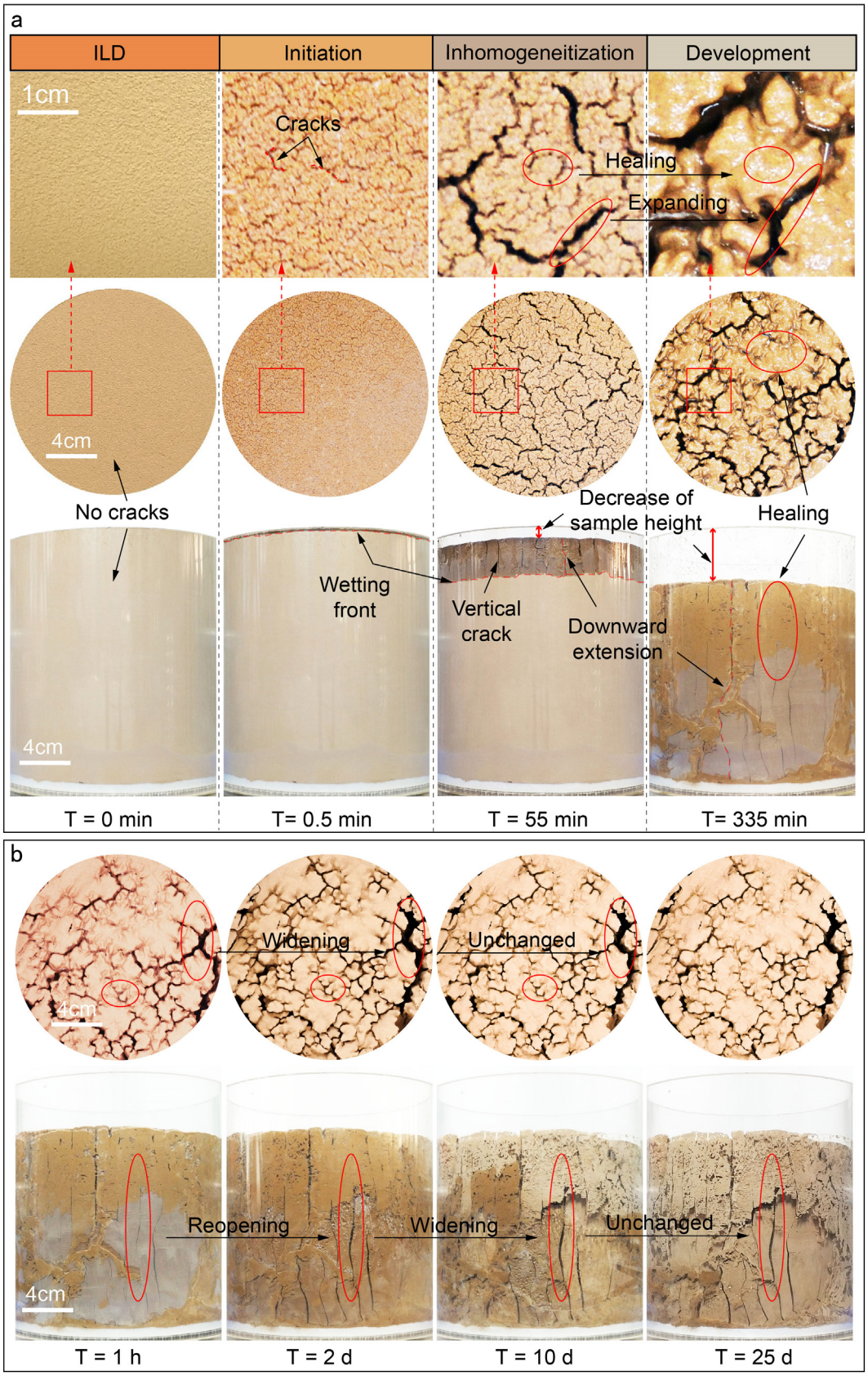

Fig. 3. Structural evolution of ILD during WD cycle as viewed from the top and sides of the sample. a, Main stages of ILD's structural evolution during wetting (crack initiation, inhomogeneitization, and development). b, Structural evolution during drying.

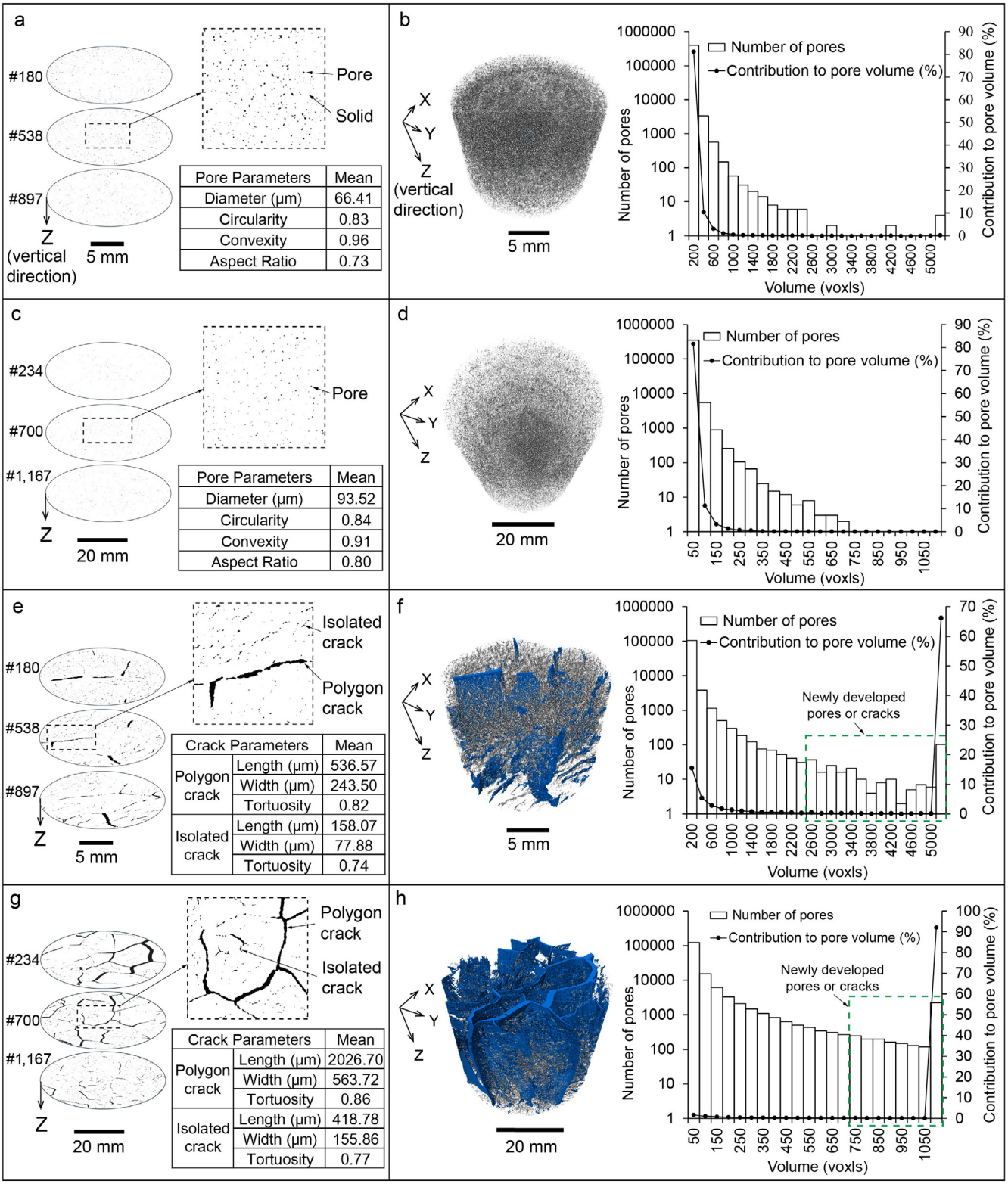

Fig. 4. 2D and 3D structural characteristics of ILD extracted from CT images before and after WD process. a,b, Pre-WD specimen ILD-2 (2 cm in diameter and 2 cm in height). c,d, Pre-WD specimen ILD-5 (5 cm in diameter and 5 cm in height). e,f, Post-WD specimen WD-2. g,h, Post-WD specimen WD-5. The first column of figures (a,c,e,g) summarize 2D structural characteristics, where tables present the mean values of 2D structural parameters of pores and cracks. The symbol "#" represents the number of the slices counted from top to bottom. The second column of figures (b,d,f,h) present (1) 3D structural reconstruction of pores and cracks (left): pores and cracks developed in WD process are in blue color; and (2) bar charts (right) of the numbers of pores and cracks in each size range and their contribution to the total pore volume. In the bar charts, 2400 voxels and 700 voxels were set as thresholds to recognize the newly developed pores or cracks in Post-WD specimens, WD-2 and WD-5, respectively, because such big pores or cracks were rarely found in Pre-WD specimens, ILD-2 and ILD-5. (For interpretation of the references to color in this figure legend, the reader is referred to the web version of this article.)

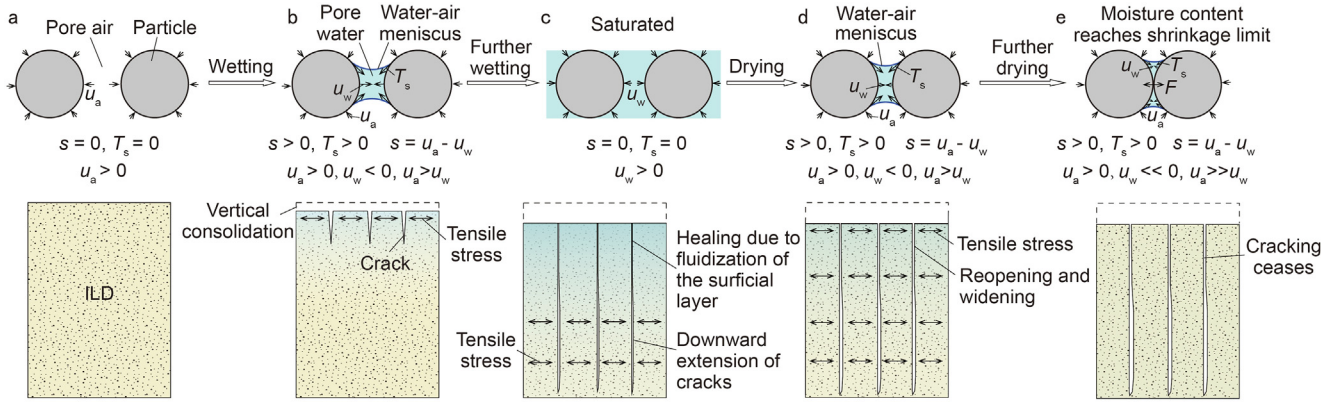

Fig. 5. Formation of vertical cracks during a wetting-drying cycle at particle (upper row) and sample (lower row) scales. a, Original ILD. b, Water-air meniscus formed between loess particles during wetting, generating matric suction (s, $s = u_a - u_w$, u_a: pore air pressure; u_w: pore water pressure) and surface tension (T_s). Vertical cracks initiated due to tensile stress developed in the wetted zone. c, With continued wetting, the cracks extended downward with the wetting front, while their initial segments in the upper zone healed due to fluidization. d, With the onset of drying, water-air meniscus was regenerated between the particles, leading to reopening of the healed segments and further widening of the open segments of the cracks. e, When the soil reached its shrinkage limit with further drying, crack expansion ceased as the inter-particle forces (s, T_s, and F) attained equilibrium.

greater than 0.9 (Fig. 4a,c). Spatially, the pores were isolated from each other and evenly distributed (Fig. 4b,d).

Upon subject to WD, the ILD became denser and anisotropic, and cracks developed extensively (Fig. 3; see Supplementary Video). The top and side views in Fig. 3a revealed the following three key stages in ILD structural evolution:

(1) Crack initiation. At this stage, tension cracks appeared extensively at the top of ILD. These cracks, with approximate width of 0.5 mm and length of 4 mm, were evenly distributed on the top surface and tended to intersect each other to form 5–6 sided polygons that had an average area of 0.16 cm^2 and area density of 640 no./dm^2. There was no obvious structural change along the side of the ILD.
(2) Crack inhomogeneitization. In this stage, some cracks grew wide and long and connected with each other to form large polygons, while the cracks within the polygons basically remained unchanged, forming an inhomogeneous pattern. The large polygons are about 25 times the original small ones. The cracks forming large polygons propagated in the vertical or sub-vertical direction. The cracks exposed on the side were generally parallel to each other at a spacing of approximately 1 cm (Fig. 3a). The downward extension of these cracks kept in step with the downward migration of wetting front.
(3) Crack development. From the top view, the large cracks continued to expand both in width and length, and the cracks inside the large polygons narrowed and eventually healed up as the soil was gradually saturated from the top. As a result, the inhomogeneity of the soil was enhanced. From the side view, cracks in the upper saturated layer started to heal, while cracks in the unsaturated zones continued to extend downwards.

In the subsequent drying process, the aperture of large cracks further increased and the healed cracks tended to reopen (Fig. 3b; see Supplementary Video). This phenomenon proceeded from top to bottom of the sample and ceased after 10 days of drying when the sample reached its shrinkage limit. No obvious change in cracks was monitored upon further drying to make the specimen completely dry.

3.2. Creating prototype loess structure

During the entire WD process, the height of the ILD progressively decreased (Fig. 3), leading to post-WD samples with much denser (overall density of 1.12 g/cm^3) soil mass than the pre-WD samples (density of 0.88 g/cm^3). Compared to the latter (ILD-5 and ILD-2) (Fig. 4b,d), a huge number of large pores and cracks, accounting for a great proportion of the total pore volume, were detected in the former (WD-5 and WD-2) (Fig. 4f,h). This suggests that WD reduced isolated small pores, and caused them to join together to form large pores and cracks (Fig. 4f,h).

The structural characteristics of pores and cracks in the post-WD samples are shown in Fig. 4e–h. Most pores were spherical and evenly distributed and the cracks were well-developed forming a polygonal-crack-network structure. As shown in the 5-cm specimen (Fig. 4g,h), some cracks joined to form 5–6 sided polygons, while within polygons, isolated cracks prevailed. These isolated cracks are generally narrower, shorter, and more curved than the cracks forming the polygons (Fig. 4e,g). Both polygon cracks and isolated cracks are oriented vertically or sub-vertically (Fig. 4f,h). The post-WD structure of ILD with its weak segments consisting mainly of cracks and compact blocks bounded by these cracks is comparable to the present-day loess structure.

Comparison of the crack patterns at different stages in Fig. 3a shows that the final structure (Fig. 4e-h) first appeared during the crack inhomogeneitization stage (Fig. 3a), and the cracks that healed up during the crack development stage reopened in the subsequent drying process (Fig. 3b). This suggests that the crack pattern of the inhomogeneitization stage is stable and can therefore be taken to represent the prototype of the present-day loess structure.

4. Discussion

Most previous studies on loess structure evolution were on present-day undisturbed and compacted loess samples. These studies suggest that drying-induced shrinkage was the main cause for the formation of vertical cracks (Li et al., 2014; Lu et al., 2015; Peth et al., 2010). A further suggestion is that polygonal-crack-network structures are caused by drying shrinkage. Specifically, the ILD collapses under wetting and/or loading and this leads to particle rearrangement and soil densification. Subsequent drying process then modifies the matrix suction and generates tensile stress to form a network of cracks (Smalley et al., 2016). Results of our study showed that drying-induced shrinkage contributes to the formation of cracks only to some extent, where the wetting process has a dominant role: the polygonal-crack-network which forms during wetting are reopened and/or widened during drying.

Before wetting, the ILD was in a dry state and the forces acting on the particles were in equilibrium (Fig. 5a). At the beginning of wetting, the surficial layer of soil became wet but unsaturated, and water-air

meniscus formed between particles, leading to the development of matric suction (s) and surface tension (T_s) (Fig. 5b). The matric suction and surface tension tended to pull the soil particles closer to each other (Fredlund and Rahardjo, 1993; Li et al., 2014; Lu and Likos, 2004; Luan et al., 2006). As the ILD had only few contacts between particles and lacked cohesive inter-particle bonds (Peth et al., 2010; Smalley et al., 2016), the horizontal tensile stress induced by matric suction and surface tension could easily re-arrange particles and cause cracking at weaker points (Fig. 5b). Due to the homogeneity of ILD, cracking occurs almost simultaneously, forming a relatively regular network (Smalley, 1966). Beside the matric suction and surface tension, other inter-particle forces, such as van der Waals force, charge force and osmotic suction, may also contribute to the development of tensile stress during wetting, but they play a minor role (Li et al., 2014; Lu and Likos, 2004; Tang et al., 2018). The soil also shrank in the vertical direction (Fig. 5b) mainly because of the increase of soil weight caused by the addition of water. With further wetting, the cracks extended vertically as the tension stress was developed with the downward migration of water (Fig. 5c). On the other hand, continuous wetting caused the top layer to become fluidized, healing up some of the cracks (Fig. 5c), where the matrix suction (s) and surface tension (T_s) decreased or even disappeared.

As drying proceeded, the soil gradually returned to unsaturated state. Matric suction and surface tension recovered with the decrease in moisture content (Fig. 5d). This led to further soil contraction, which in turn resulted in the widening and lengthening of existing cracks (Wackertapp et al., 2000), reopening of healed cracks, and development of small-scale cracks (Fig. 5d). Once the moisture content decreased to the shrinkage limit of the soil (Luan et al., 2008; Tang et al., 2011), crack expansion ceased and the pore volume remained basically unchanged with further drying as the resultant force of non-contact forces (s and T_s) was balanced with the contact force (F) (Fig. 5e). The crack network after the drying process was the same as that formed in the inhomogeneitization stage (Figs. 3 and 4), indicating that the development of matric suction and surface tension due to wetting primarily caused the formation of cracks, while later drying just slightly modified the crack pattern.

Based on the TTR III multifunctional X-ray diffractometer test, the clay minerals in the sample of the present study are mainly composed of interstratified illite/smectite, illite, kaolinite and chlorite, with relative percentages of 50%, 24%, 16% and 10%, respectively. Clay minerals may swell or shrink with water variation (Tang et al., 2011). However, the ILD sample kept shrinking during the wetting process. This is opposite to the swelling effect of clay minerals and indicates that clay minerals may not play a dominant role in structure evolution in WD process.

Other environmental factors, such as freezing-thawing and temperature cycles, and chemical factors can also modify soil structure (Keith and Peter, 1982). In particular, the ice-water phase transformation caused by freezing-thawing cycles weakens bonding between soil particles and leads to fragmentation of loess aggregates (Li et al., 2018a). The temperature cycles may cause volumetric change (expansion or contraction) of soil particles, and therefore changes the structure of loess (Campanella and Mitchell, 1968). The dissolution of soluble salt may lead to disintegration of loess (Zhang et al., 2013, 2014; Li et al., 2017). However, relevant retrievable findings are mainly on undisturbed present-day loess or remoulded loess samples, and therefore cannot explain how the initial loess deposit (ILD) evolves into the present structure. The present paper took ILD as the initial point and recognized the important role the wetting-drying process plays in the structural evolution of ILD. We speculate that other environmental and chemical factors may have effects in the structural evolution of ILD. This, however, requires detailed future studies with specified test programs.

According to previous researches, the first WD cycle plays the most important role in case of structure formation and more WD cycles just cause little alteration of soil structure (Bryant, 1989; Tang et al., 2011). Furthermore, it took a quite long time of more than three months in the laboratory to complete one WD cycle. Considering the above, this paper mainly focuses on the first WD cycle. In addition, it is meaningful to catch the variation of matric suction, pore water pressure and moisture content of the sample during WD process. However, the fabricated analogs of ILD was extremely loose and it was not possible to install any sensors to monitor these parameters. To cover the above issues, a further study with specified test setup and program is required.

5. Conclusions

In this study, we carried out wetting-drying (WD) experiments on fabricated analogs of initial loess deposits (ILD) to simulate the evolution of loess structure. Our results showed that the free-fall method produced a deposit with loose and homogeneous structure, representing ILD. The pores in the samples were nearly spherical, isolated, and evenly distributed. Upon being subjected to WD, the ILD had undergone three stages of structural evolution - crack initiation, inhomogeneitization, and development - in the process of which the deposit gradually became denser and eventually achieved an anisotropic structure characterized by vertically aligned cracks separating densely packed loess blocks. This prototype structure is consistent with the vertiloess structure of present-day loess. Comparison of structures at different stages of the evolution indicates that, contrary to the common belief, it is the wetting rather than drying that initiates and drives the structural evolution while drying preserves and expands the structures created by the wetting process.

Declaration of Competing Interest

The authors declare that they have no known competing financial interests or personal relationships that could have appeared to influence the work reported in this paper.

Acknowledgements

This study was supported by the Key Program of National Natural Science Foundation of China (No. 41630640), Major Program of the National Natural Science Foundation of China (No. 41790445), and National Natural Science Foundation of China (No. 41877276). The authors are grateful to Prof. Z. Guo of Taiyuan University of Technology, and Dr. M. A. Beroya-Eitner of Technische Universität Darmstadt for their valuable suggestions and in-depth review of the manuscript.

Appendix A. Supplementary data

Supplementary data to this article can be found online at https://doi.org/10.1016/j.geoderma.2020.114564.

References

Assallay, A.M., Rogers, C.D.F., Smalley, I.J., 1997. Formation and collapse of metastable particle packings and open structures in loess deposits. Eng. Geol. 48 (1), 101–115. https://doi.org/10.1016/S0013-7952(97)81916-3.

Balsam, W., Ji, J., Chen, J., 2004. Climatic interpretation of the Luochuan and Lingtai loess sections, China, based on changing iron oxide mineralogy and magnetic susceptibility. Earth Planet. Sc. Lett. 223 (3–4), 335–348. https://doi.org/10.1016/j.epsl.2004.04.023.

Berg, L.S., 1916. The origin of loess. Izvestiya Russkogo Geograficheskogo Obshchestva 52, 579–646.

Bryant, R.B., 1989. Physical Processes of Fragipan Formation. SSSA Special Publication, Madison.

Campanella, R.G., Mitchell, J.K., 1968. Influence of temperature variation on soil behavior. Journal of the Soil Mechanics & Foundations Division 94 (3), 609–734.

Ding, Z.L., Yu, Z.W., Yang, S.L., Sun, J.M., Xiong, S.F., Liu, T.S., 2001. Coeval changes in grain size and sedimentation rate of eolian loess, the Chinese Loess Plateau. Geophys. Res. Lett. 28 (10), 2097–2100. https://doi.org/10.1029/2000gl006110.

Fredlund, D.G., Rahardjo, H., 1993. Soil Mechanics for Unsaturated Soils. John Wiley and Sons, New York https://doi.org/10.1002/9780470172759.
Gao, G.R., 1988. Formation and development of the structure of collapsing loess in China. Eng. Geol. 25, 235–245. https://doi.org/10.1016/0013-7952(88)90029-4.
Kapur, J.N., Sahoo, P.K., Wong, A.K.C., 1985. A new method for gray-level picture thresholding using the entropy of the histogram. Comput. Vision Graph. Image Process. 29, 273–285. https://doi.org/10.1016/0734-189X(85)90125-2.
Keith, B., Peter, G., 1982. Macropores and water flow in soils. Water Resour. Res. 18 (5), 1311–1325. https://doi.org/10.1029/wr018i005p01311.
Li, G.Y., Wang, F., Ma, W., Richard, F., Mu, Y.H., Mao, Y.C., Hou, X., 2018a. Variations in strength and deformation of compacted loess exposed to wetting–drying and freeze–thaw cycles. Cold Reg. Sci. Technol. 151, 159–167. https://doi.org/10.1016/j.coldregions.2018.03.021.
Li, S., Xu, Q., Zhang, L.Z., Peng, D.L., Lü, H.B., Song, S.J., 2017. Time effect and mechanism of strength weakening of loess soaked in water in Heifangtai area. Rock and Soil Mechanics 38 (7), 2043–2048, 2058. https://doi.org/10.16285/j.rsm.2017.07.026.
Li, T.L., Wang, H., Fu, Y.K., Liang, Y., 2014. Test Simulation on the forming mechanism of loess vertical joints. J. Earth Sci. Environ. 36 (2), 127–134. https://doi.org/10.3969/j.issn.1672-6561.2014.02.018.
Li, X.A., Li, L.C., 2017. Quantification of the pore structures of Malan loess and the effects on loess permeability and environmental significance, Shaanxi province, China: an experimental study. Environ. Earth Sci. 76 (15), 523. https://doi.org/10.1007/s12665-017-6855-7.
Li, Y.R., He, S.D., Deng, X.H., Xu, Y.X., 2018b. Characterization of macropore structure of Malan loess in NW China based on 3D pipe models constructed by using computed tomography technology. J. Asian Earth Sci. 154, 271–279. https://doi.org/10.1016/j.jseaes.2017.12.028.
Li, Y.R., Zhang, T., Zhang, Y.B., Xu, Q., 2018c. Geometrical appearance and spatial arrangement of structural blocks of the Malan loess in NW China: implications for the formation of loess columns. J. Asian Earth Sci. 158, 18–28.
Li, Y.R., Zhang, W.W., Aydin, A., Deng, X.H., 2018d. Formation of calcareous nodules in loess–paleosol sequences: reviews of existing models with a proposed new “per evapotranspiration model. J. Asian Earth Sci. 154, 8–16. https://doi.org/10.1016/j.jseaes.2017.12.002.
Liu, T.S., 1985. Loess and Environment. Science press, Beijing.
Liu, Z.F., Wei, G.J., Wang, X.S., Jin, C.S., Liu, Q.S., 2016. Quantifying paleoprecipitation of the Luochuan and Sanmenxia loess on the Chinese Loess Plateau. Palaeogeogr. Palaeocl. 459, 121–130. https://doi.org/10.1016/j.palaeo.2016.06.034.
Lu, H.J., Li, J.X., Wang, W.W., Wang, C.H., 2015. Cracking and water seepage of Xiashu loess used as landfill cover under wetting–drying cycles. Environ. Earth Sci. 74 (11), 1–10. https://doi.org/10.1007/s12665-015-4729-4.
Lu, N., Likos, W.J., 2004. Unsaturated Soil Mechanics. Wiley, New York.
Luan, M.T., Li, S.Q., Yang, Q., 2006. Matric suction and tension suction of unsaturated soils. Chinese J. Geotech. Eng. 28 (7), 863–868.
Luan, M.T., Wang, D.L., Yang, Q., Li, P.Y., 2008. Experimental study on drying shrinkage of unsaturated compacted soils. Chinese J. Geotech. Eng. 30 (1), 119–122.
Malvern Instruments Ltd, 2013. Morphologi G3 User Manual. Malvern Instruments Ltd, Worcestershire.
Meng, X.Q., Liu, L.W., Balsam, W., Li, S.L., He, T., Chen, J., Ji, J.F., 2015. Dolomite abundance in Chinese loess deposits: a new proxy of monsoon precipitation intensity. Geophys. Res. Lett. 42 (23), 10391–10398. https://doi.org/10.1002/2015GL066681.
Pan, D.Y., 1958. Loess. Geological Publishing House, Beijing.
Pécsi, M., 1990. Loess is not just the accumulation of dust. Quatern. Int. 7–8, 1–21. https://doi.org/10.1016/1040-6182(90)90034-2.
Peth, S., Nellesen, J., Fischer, G., Horn, R., 2010. Non–invasive 3D analysis of local soil deformation under mechanical and hydraulic stresses by μCT and digital image correlation. Soil Till. Res. 111, 3–18. https://doi.org/10.1016/j.still.2010.02.007.
Pires, L.F., Auler, A.C., Roque, W.L., Mooney, S.J., 2020. X-ray microtomography analysis of soil pore structure dynamics under wetting and drying cycles. Geoderma 362. https://doi.org/10.1016/j.geoderma.2019.114103.
Pires, L.F., Cooper, M., Cássaro, F.A.M., Reichardt, K., Bacchi, O.O.S., Dias, N.M.P., 2008. Micromorphological analysis to characterize structure modifications of soil samples submitted to wetting and drying cycles. Catena 72 (2), 297–304. https://doi.org/10.1016/j.catena.2007.06.003.
Pye, K., 1995. The nature, origin and accumulation of loess. Quaternary Sci. Rev. 14 (7), 653–667. https://doi.org/10.1016/0277-3791(95)00047-X.
Richthofen, B.F., 1882. On the mode of origin of the loess. Geol. Mag. 9 (7), 293–305. https://doi.org/10.1017/S001675680017164X.
Smalley, I.J., 1966. Contraction crack networks in basalt flows. Geol. Mag. 103 (2), 110–114. https://doi.org/10.1017/S0016756800050482.
Smalley, I.J., Bentley, S.P., Markovic, S.B., 2016. Loess and fragipans: Development of polygonal–crack–network structures in fragipan horizons in loess ground. Quatern. Int. 399, 228–233. https://doi.org/10.1016/j.quaint.2015.01.034.
Sprafke, T., Obreht, I., 2016. Loess: Rock, sediment or soil – What is missing for its definition. Quatern. Int. 399, 198–207. https://doi.org/10.1016/j.quaint.2015.03.033.
Tang, C.S., Cui, Y.J., Shi, B., Tang, A.M., Liu, C., 2011. Desiccation and cracking behaviour of clay layer from slurry state under wetting–drying cycles. Geoderma 166, 111–118. https://doi.org/10.1016/j.geoderma.2011.07.018.
Tang, C.S., Shi, B., Cui, Y.J., 2018. Behaviors and mechanisms of desiccation cracking of soils. Chinese J. Geotech. Eng. 40 (8), 1415–1423.
Wackertapp, J., Hergarten, S., Neugebaue, H.J., 2000. A model for propagation and concentration of microcracks. Geophys. Res. Lett. 27 (12), 1771–1774. https://doi.org/10.1029/1999gl010476.
Xu, X.X., Kalhoro, S.A., Chen, W.Y., Raza, S., 2017. The evaluation/application of Hydrus–2D model for simulating macro–pores flow in loess soil. Int. Soil Water Conser. Res. 5 (3), 196–201.
Zhang, F.Y., Wang, G.H., Kamai, T., Chen, W.W., 2014. Effect of pore-water chemistry on undrained shear behaviour of saturated loess. Q. J. Eng. Geol. Hydroge. 47, 201–210. https://doi.org/10.1144/qjegh2013-085.
Zhang, F.Y., Wang, G.H., Kamai, T., Chen, W.W., Zhang, D.X., Yang, J., 2013. Undrained shear behavior of loess saturated with different concentrations of sodium chlorate solution. Eng. Geol. 155, 69–79. https://doi.org/10.1016/j.enggeo.2012.12.018.